Vacuum-Assisted Thermal Annealing of $CH_3NH_3PbI_3$ for Highly Stable and Efficient Perovskite Solar Cells

Feng Xian Xie,[†] Di Zhang,[†] Huimin Su,[‡] Xingang Ren,[†] Kam Sing Wong,[‡] Michael Grätzel,[§] and Wallace C. H. Choy*,[†]

[†]Department of Electrical and Electronic Engineering, The University of Hong Kong, Pok Fu Lam Road, Hong Kong, China, [‡]Department of Physics, The Hong Kong University of Science & Technology, Clear Water Bay, Kowloon, Hong Kong, and [§]Laboratory for Photonics and Interfaces, Institute of Chemical Sciences and Engineering, School of Basic Sciences, Ecole Polytechnique Fédérale de Lausanne, CH-1015 Lausanne, Switzerland

ABSTRACT Solar cells incorporating lead halide-based perovskite absorbers can exhibit impressive power conversion efficiencies (PCEs), recently surpassing 15%. Despite rapid developments, achieving precise control over the morphologies of the perovskite films (minimizing pore formation) and enhanced stability and reproducibility of the devices remain challenging, both of which are necessary for further advancements. Here we demonstrate vacuum-assisted thermal annealing as an effective means for controlling the composition and morphology of the $CH_3NH_3PbI_3$ films formed from the precursors of $PbCl_2$ and CH_3NH_3I. We identify the critical role played by the byproduct of CH_3NH_3Cl on the formation and the photovoltaic performance of the perovskite film. By completely removing the byproduct through our vacuum-assisted thermal annealing approach, we are able to produce pure, pore-free planar $CH_3NH_3PbI_3$ films with high PCE reaching 14.5% in solar cell device. Importantly, the removal of CH_3NH_3Cl significantly improves the device stability and reproducibility with a standard deviation of only 0.92% in PCE as well as strongly reducing the photocurrent hysteresis.

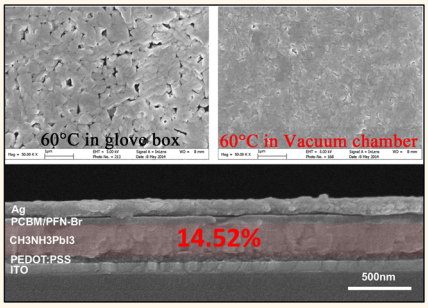

KEYWORDS: perovskite solar cell · vacuum-assisted thermal annealing · CH_3NH_3Cl · morphology · crystallization process

Low-temperature, solution-processable solar cells have become very attractive because they can be manufactured cost-effectively on large scales and with high throughput.[1−5] Recently, methylammonium lead halide perovskites ($CH_3NH_3PbI_3$) have been identified as promising absorbers for solar cell applications with very impressive power conversion efficiencies (PCEs) of over 15%,[6−10] due to their remarkable long-range, balanced electron and hole transport diffusion lengths and their bipolar charge transport capabilities.[11−14] Previous studies of high-efficiency perovskite solar cells have often made use of (mesoscopic) metal oxides, such as Al_2O_3, TiO_2, and ZnO,[15−18] which require high-temperature sintering to form a scaffold structure. Structures with a planar junction have also been reported,[19−24] where the perovskite film is sandwiched between selective electrodes, obviating the need for a nanostructured (scaffold) electron acceptor and simplifying the device processing procedure.

CH_3NH_3I and $PbCl_2$ mixture are the most commonly used materials in the deposition solution in one step planar structures.[21−23] The $3CH_3NH_3I$:$PbCl_2$ precursor, rather than forming the mixed halide $CH_3NH_3PbI_{3-x}Cl_x$, yields pure $CH_3NH_3PbI_3$ perovskite accompanied by the release of gaseous CH_3NH_3Cl (MACl) (or other organic chlorides in a similar form) byproduct, as indicated by the weak Cl signal in the bulk perovskite films.[25,26] Since the crystallization process of $CH_3NH_3PbI_3$ can be controlled during the phase of forming intermediate organometal mixed halide, the photovoltaic properties of the perovskite films are typically superior to those of films formed directly in one step precipitation process from a CH_3NH_3I and PbI_2 mixture.[12,27] Nevertheless, controlling the crystallization process of perovskite films remains a challenging issue. The $CH_3NH_3PbI_3$ perovskite crystallization from the $3CH_3NH_3I$:$PbCl_2$ precursor is found to be strongly affected by the ambient, which in turn can compromise the performance and

* Address correspondence to chchoy@eee.hku.hk.

Received for review October 20, 2014 and accepted December 30, 2014.

Published online December 30, 2014
10.1021/nn505978r

reproducibility of the perovskite device. For instance, while ambient moisture has been reported to detrimentally affect the structure and stability of the perovskite,[28] a humidity-controlled environment has also been reported to facilitate the crystallization of perovskite films.[29] In addition, in a glovebox, gases and vapors released during film formation (*e.g.*, solvent vapor from the perovskite precursor solution) are also difficult to control, which may affect the perovskite crystallization. Therefore, an effective approach for enhancing the morphology of perovskite films through controlling their crystallization process is highly desired.

In this study, we propose a vacuum-assisted thermal annealing method for providing favorable environment for effectively controlling the crystallization of the perovskite films. Besides confirming the generation of MACl byproduct, our studies indicate that MACl plays a critical role during the perovskite film formation and device degradation. By promoting the release of MACl and suppressing residual MACl in the film through the vacuum-assisted thermal annealing, we are able to obtain pore-free and well crystallized pure triiodide ($CH_3NH_3PbI_3$) perovskite films that contained no residual chloride species. As a result, we realize highly stable and efficient solar cells displaying excellent reproducibility (13.60 $\pm$ 0.92% among 60 devices; highest PCE: 14.52%) and a very small photocurrent hysteresis effect. We believe that this approach will also enable further improvements in the performance of related perovskite materials.

RESULTS AND DISCUSSION

The Importance of MACl Release Rate in Perovskite Formation. Starting with CH_3NH_3I (MAI) and $PbCl_2$ as mixed precursors in a 3:1 molar ratio (hereafter referred to as "3MAI:$PbCl_2$"), the overall stoichiometry of the conversion reaction is as follows[25] (intermediate phase during the reaction is omitted):

$$3CH_3NH_3I + PbCl_2 \rightarrow CH_3NH_3PbI_3 + 2CH_3NH_3Cl\,(MACl)\uparrow \quad (1)$$

During the reaction, a chloride compound with the chemical composition of MACl is generated. We confirmed the generated MACl by performing XPS analysis on the white mist collected during the thermal annealing process of the perovskite precursor, which contained compound signals for chlorine, carbon and nitrogen atoms [Supporting Information Figure S1].

At the onset of the conversion reaction 1, MACl is generated at a certain rate upon thermal annealing. Here, we find that achieving a faster release rate than the generation rate of MACl is key for preventing pore formation in perovskite films. To fulfill this requirement, we introduce a vacuum-assisted thermal annealing (VATA, see Methods section for details) approach as a means for controlling the removal of the MACl byproduct.

To illustrate the importance of the MACl release rates during the crystallization of pore-free $CH_3NH_3PbI_3$ perovskite, we thermally annealed samples prepared from the 3MAI:$PbCl_2$ solutions separately in a vacuum chamber and in a glovebox. First, we observed the color of the film changed from yellow to red-brown upon annealing concurrently with crystallization. Therefore, we could correlate the rate of color change to that of the crystallization. We found that the vacuum condition of thermal annealing, which determines the release rate of MACl by vaporization, strongly affects the crystallization time of $CH_3NH_3PbI_3$ films. It has been reported that $3CH_3NH_3I$:$PbCl_2$ film with poly(methyl methacrylate) coating (preventing the release of MACl) showed little changes in color even after high temperature thermal annealing for long period.[26] In our experiment, as revealed in Figure 1a,b, the crystallization time of the perovskite film in a glovebox was 80 min when annealed at 60 °C. In the vacuum chamber, the crystallization time of the perovskite films decreased to 30 min when annealed at the same temperature. Therefore, the release of MACl byproduct, which leaves room for the perovskite, significantly accelerates the perovskite crystallization process.

It should be noted that the humidity levels during film formation can also considerably affect the crystallization rate of the perovskite films, which were specifically excluded from our vacuum and nonvacuum devices for rational comparison of the MACl byproduct: the humidity level in our glovebox and vacuum chamber was strictly controlled to less than 1 ppm. As a reference, we added 3% H_2O into the perovskite precursor solution, and observed the crystallization time at 60 °C in glovebox greatly increased to ~10 h. We have also fabricated perovskite films in air (with certain humidity) and observed different morphologies compared to films formed in glovebox and in vacuum [SEMs pictures of the samples are shown in Supporting Information Figures S4−S6]. Because of its high sublimation point of about 200 °C,[30] the release of MACl can happen at annealing temperature higher than ~170 °C.[30] We deduce that the MACl released from the film could be in the form of MA and HCl gas state molecules. These MA and HCl gas state molecules can convert to solid state MACl when they recombine. The solvent, *e.g.*, H_2O, would retain these molecules, making the escape of MACl harder than that of the moisture-free samples.

More importantly, we found that the morphologies of the films thermally annealed in the glovebox [Figure 1a] and vacuum chamber [Figure 1b] were considerably different. *In the former case*, the annealed films generally featured loosely packed, larger crystals surrounding pores. Here, we attribute the morphological features, *i.e.*, crystal size and pore structure of the perovskite to the accumulation of the MACl byproduct,

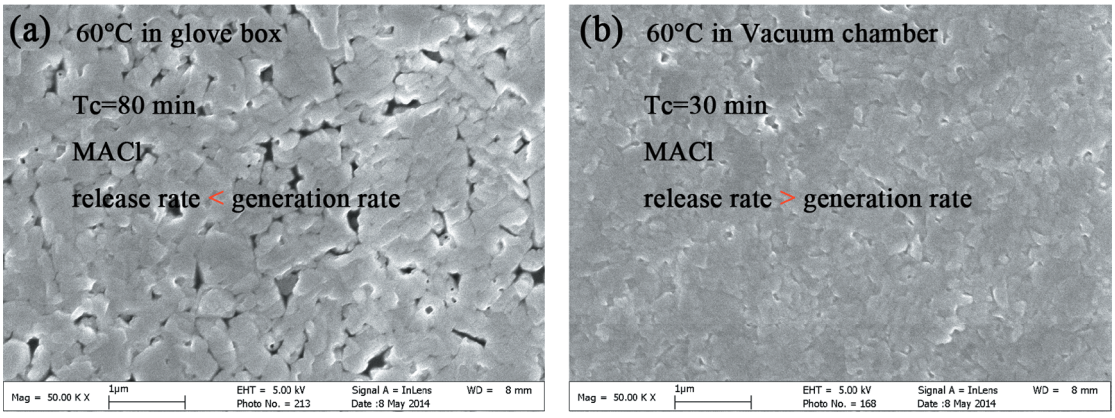

Figure 1. SEM images of the top surfaces of perovskite films. SEM images of perovskite films obtained from 3MAI:$PbCl_2$ precursor, formed on PEDOT:PSS/ITO glass substrates, after thermal annealing in (a) a glovebox and (b) a vacuum chamber at 60 °C.

which may be driven by the thermal kinetics within the perovskite film. The accumulation of the MACl byproduct is controlled by the ratio of generation rate *versus* the release rate of MACl. From reaction 1, it can be inferred that an increase in the annealing temperature would favor the forward reaction, such that the rate of generation of MACl would increase. At low annealing temperature (60 °C) in glovebox, small pores are formed as shown in Figure 1a. Due to the high sublimation point of 195 °C, the release rate of MACl in ambient pressure is very small. Here, the balance of MACl is dominated by MACl generation, leading to moderate accumulation of MACl. The moderately aggregated MACl thus left small pores after thermal annealing. For the samples thermally annealed at higher temperatures, the generation of MACl increased further, giving rise to MACl accumulation to a greater extent. As a result, we could observe crystals of larger size (Supporting Information Figure S4). In contrast, when the films were annealed in vacuum at 60 °C, the sublimation point of MACl decreased upon decreasing the pressure, thereby facilitating the release of MACl. The MACl release rate thus exceeds that of generation, which can effectively suppress MACl aggregation in the film. Such an environment enables the perovskite to grow into a compact, pore-free, and better crystallite structure at 60 °C in vacuum [Figure 1b]. Therefore, it can be concluded that the key for obtaining condensed and pore-free film is a controlled balance of MACl where the release rate is greater than the generation rate. Due to the high sublimation point of MACl, achieving such a criterion under ambient pressure (in glovebox) is very difficult. However, under vacuum, it can be easily realized by the VATA approach.

Next, we studied the surface roughness of the films prepared *via* the VATA method. The AFM image in Figure 2a reveals formation of a smooth film having a root-mean-square roughness of 9.59 nm for a film thickness of 300 nm. The AFM measurement was carried out over an area of 5 μm^2, which was chosen randomly from a large and uniform VATA film. The uniformity of the large-area film was confirmed by SEM [Supporting Information Figure S9], which could ensure minimal uncertainty in our measurement. The corresponding root-mean-square roughness of perovskite film in glovebox is 12.4 nm [Supporting Information Figure S7a]. From the phase image of the perovskite film in Figure 2b, we observed that small crystals were formed their quality being comparable to that of evaporated $CH_3NH_3PbI_3$ films.[7,31] Figure S8 in Supporting Information displays the morphologies of samples of various thicknesses (300, 250, 200, and 100 nm) that had been subjected to an annealing temperature of 60 °C in the vacuum chamber. In each case, we obtained the same smooth, pore-free film, suggesting that such vacuum annealing is a very efficient and reproducible method for different processing conditions. The excellent compactness of the perovskite films was also revealed from the real and imaginary parts of the refractive index *n* and *k*, respectively [Supporting Information Figure S17a]. The derived absorption length is given in Supporting Information Figure S17b. The real part of the refractive index of the thermally annealed perovskite film reached as high a value as 2.86 at 520 nm, while the absorption length at 600 nm is 235 nm. The measured high refractive indices are comparable with, or even higher than values previously reported,[32] indicating that our films are compact. Consequently, by balancing the rates of generation and release of MACl through a combination of thermal and vacuum treatment, we could obtain smooth, pore-free perovskite films exhibiting high refractive indices and extinction coefficients.

Highly Stable and Efficient Solar Cells with Excellent Reproducibility and Very Little Photocurrent Hysteresis. To demonstrate that our pore-free $CH_3NH_3PbI_3$ film would be an efficient light harvester for solar cells, we prepared a simple device structure using typical organic semiconductors[19,33] as selective electron and hole extracting materials; as displayed in Figure 2c,

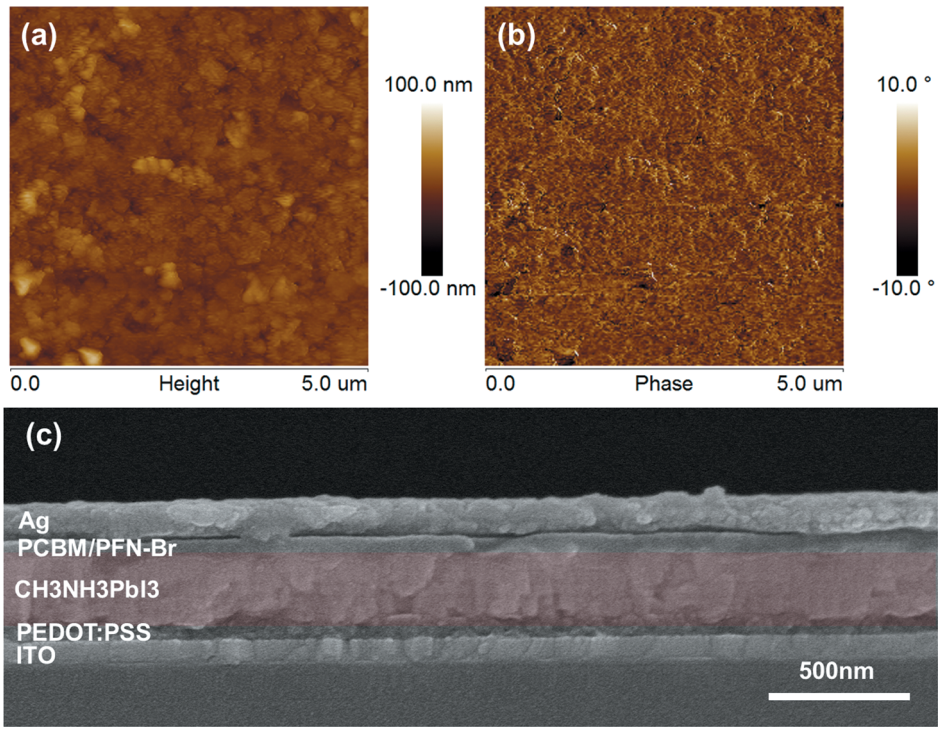

Figure 2. Top-surface AFM images of perovskite films and cross-sectional SEM images of complete perovskite device. (a and b) AFM (a) topographic and (b) phase images of the surface of a perovskite film formed on a PEDOT:PSS/ITO glass substrate and thermally annealed in a vacuum chamber at 60 °C. (c) Cross-sectional SEM image of perovskite device having the structure ITO/PEDOT:PSS/$CH_3NH_3PbI_3$/PCBM/PFN-Br/Ag.

the embodiment was indium tin oxide (ITO)/poly-(3,4-ethylenedioxythiophene):polystyrenesulfonate (PEDOT:PSS, 50 nm)/spin-coated $CH_3NH_3PbI_3$/6,6-phenyl-C_{61}-butyric acid methyl ester (PCBM, 50 nm)/poly(9,9-bis(3′-(*N*,*N*-dimethyl)-*N*-ethylammonium-propyl-2,7-fluorene)-*alt*-2,7-(9,9-dioctylfluorene))dibromide (PFN-Br)/Ag (100 nm). Here, we used PFN-Br to decrease the Schottky barrier between PCBM and Ag and, thereby, greatly enhance the electron extraction from the perovskite solar cell (see Supporting Information Figure S14). We performed device optimization over 200 independent pure-triiodide ($CH_3NH_3PbI_3$) films prepared from the mixed CH_3NH_3I and $PbCl_2$ precursor. Supporting Information Figure S12 and Table S1 provide the device performances of 300 nm-thick $CH_3NH_3PbI_3$ solar cells prepared using different annealing temperatures. Supporting Information Figure S13 and Table S2 list the performances of device incorporating films of various thicknesses that had been prepared at 60 °C; Supporting Information Figures S18 and S19 present the corresponding absorptions of the perovskite films of various thicknesses and the incident photon-to-current efficiencies (IPCEs) of the various devices along with the short circuit photocurrents derived from integrating the IPCE over the AM1.5G solar spectrum. The good agreement between the measured and the integrated photocurrents (also shown in Supporting Information Table S2) indicates that any spectral mismatch during the measurement is negligibly small.

The most efficient devices employing a perovskite film with a thickness of 300 nm were obtained from a 3MAI:$PbCl_2$ solution having a concentration of 50% by weight, applying a spin rate between 2000 and 2500 rpm, and with vacuum thermal annealing at 60 °C. The maximum PCE was 14.30% at the forward scan [Figure 3a]; this value is comparable with those of state-of-art perovskite solar cells prepared using either solution or vacuum deposition methods.[7,31] The average performance, from 60 measured devices, corresponded to a short-circuit photocurrent density (J_{SC}) of 18.28 mA/cm^2, an open-circuit voltage (V_{OC}) of 1.02 V, and a fill factor (FF) of 0.73, leading to an PCE of 13.60% (with a standard deviation of only 0.92%) under AM1.5 solar illumination at 100 mW/cm^2 [see Figure 3c–f and Supporting Information Tables S1 and S2]. The deviation in PCE of less than 10% suggested excellent reproducibility from device to device. It should be noted that due to the very high mobility of the perovskite material, each unit of the cell was cut separately to ensure accurate measurement. We attribute the high efficiency and reproducibility to the smooth, finely crystalline, and pore-free $CH_3NH_3PbI_3$ films formed through vacuum-assisted thermal annealing. The performance of the glovebox-annealed devices [Supporting Information Figure S10] suggested that the existence of pores in the perovskite films had a much greater impact than did the crystal size.

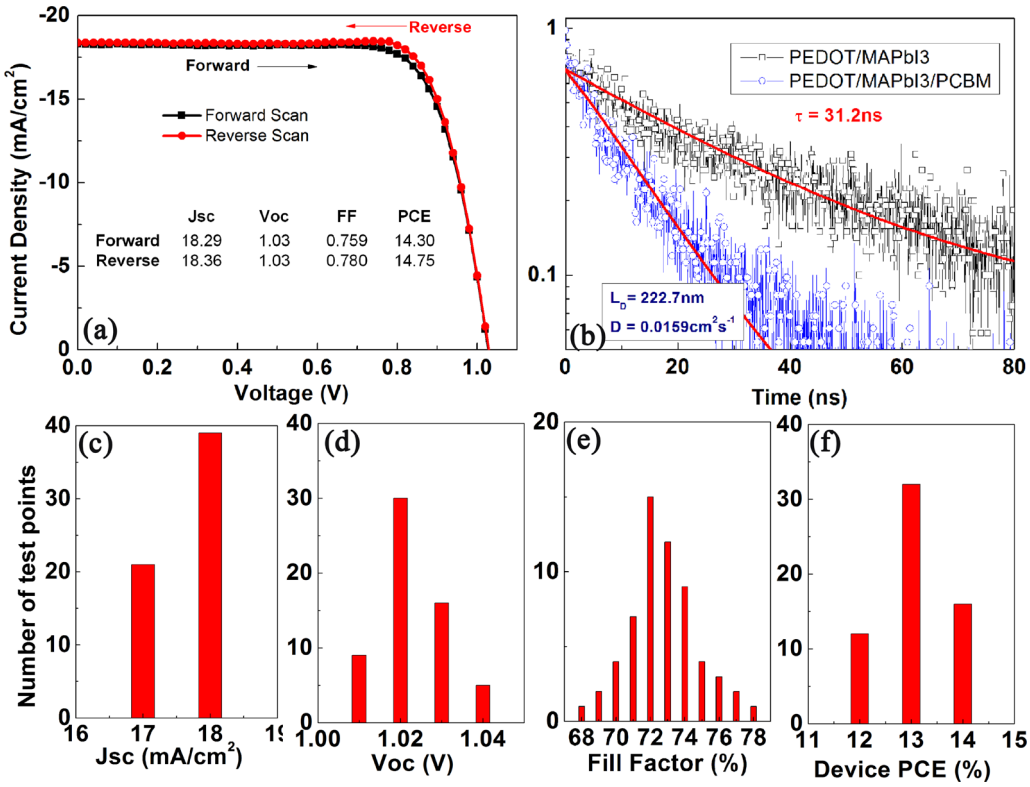

Figure 3. Characteristics of photovoltaic performance and PL behavior of a perovskite device. (a) *J*−*V* curve of the best solar cell, after forward and reverse scans with a delay time of 100 ms with a voltage step of 0.01 V. (b) PL decay measurements fitted to a single-exponential decay and diffusion model for the triiodide ($CH_3NH_3PbI_3$) in the presence and absence of PCBM quenchers. (c−f) Histograms of the solar cell reproducibility from 60 tested devices: (c) J_{sc}, (d) V_{oc}, (e) FF, and (f) PCE.

To examine the importance of a pore-free $CH_3NH_3PbI_3$ film on the various electronic properties of the perovskite materials, we performed time-resolved photoluminescence (PL) measurements to derive the electron diffusion lengths of perovskite films that we had prepared using vacuum-assisted thermal treatment. We deposited $CH_3NH_3PbI_3$ layer with a thickness of 250 nm on PEDOT:PSS support acting as hole selective contact. Figure 3b reveals that the PL decay of the neat $CH_3NH_3PbI_3$ film exhibited a time-constant (τ) of 31.2 ns, when fitted by a single exponential decay model. The addition of the PCBM electron extraction layer accelerated the PL decay, the decay kinetics of which can be analyzed by a one-dimensional diffusion model.[11,12] From the time-resolved PL decay measured at the peak emission (770 nm), we determined the electron diffusion length to be 229.7 ± 8.5 nm. Thus, the measured diffusion length of our perovskite is comparable to the reported values.[11,12] We conclude that the long carrier diffusion length in the finely crystalline, pore-free triiodide absorbers enabled the observed high photocurrent output from the corresponding solar cells.

To detect any hysteresis in the photocurrent−voltage curve, we recorded the *J*−*V* curve both in forward and reverse bias directions. The efficiency of the forward scan (14.3%) only deviated slightly from that of the reverse scan (14.75%), averaging 14.52% [Figure 3a]. Supporting Information Figure S 15 presents the effect of the scan rate on the *J*−*V* characteristics. J_{SC} and FF exhibited no substantial dependence on the scan rate, confirming the absence of any substantial hysteresis effects in our devices. Meanwhile, perovskite device thermally annealed in glovebox shows significant hysteresis effect (Supporting Information Figure S11). One cause of photocurrent hysteresis can be the presence of trapped ions within a device and from a large number of electron traps which are prone to be formed in disordered porous perovskite layers.[34] In our device, the formation of such electronic surface states is impaired by the use of organic conductor (PEDOT:PSS, PCBM/PFN-Br) as hole and electron scavenging layer, creating a smooth contact with the perovskite absorber, thereby mitigating the possibility of carrier trapping at the interface. More importantly, the pore-free perovskite layer ensured that minimal charge carriers were trapped at defect-related trap sites. Moreover, the residual chloride was removed through vacuum-assisted annealing treatment, resulting in the formation of a pure triiodide absorber; this factor contributed to decreasing the hysteresis effect caused by an excess of mobile ions within the crystal lattice.[34] Thus, vacuum-assisted processing in the perovskite solar cell resulted in both high performance and diminished photocurrent hysteresis.

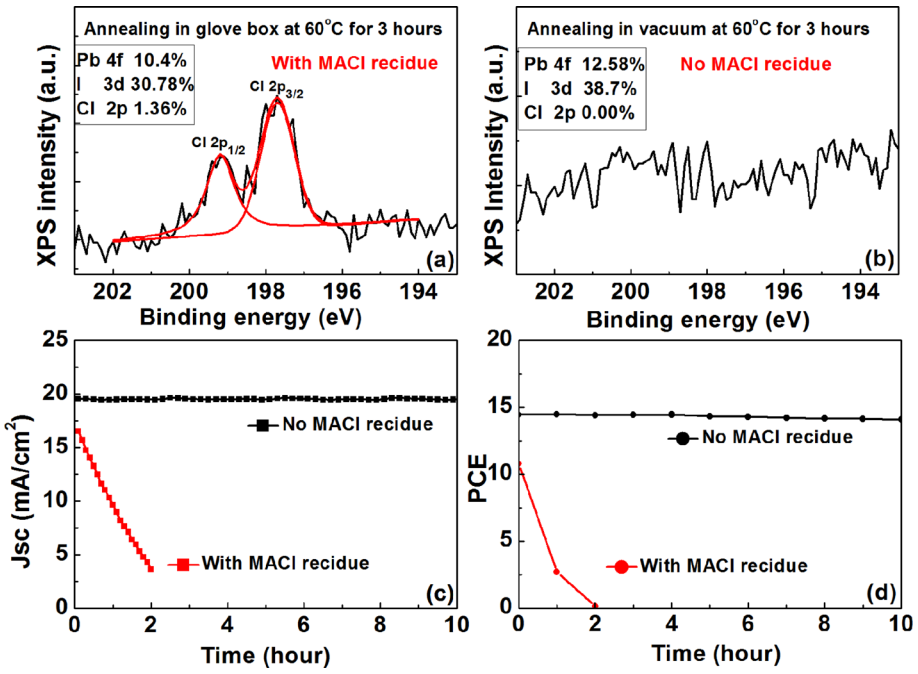

Figure 4. XPS spectra (Cl 2p core level) of (a) a perovskite film derived from 3MAI:$PbCl_2$ precursor with thermal annealing at 60 °C in a glovebox, (b) a perovskite film derived from 3MAI:$PbCl_2$ precursor with thermal annealing at 60 °C under vacuum. (c and d) Stability of a perovskite photovoltaic devices with and without MACl recidue. The device structure was ITO/PEDOT:PSS/$CH_3NH_3PbI_3$/PCBM/PFN-Br/Ag. The perovskite film incorporating MACl residue was prepared with thermal annealing at 60 °C for 2 h in a glovebox (no vacuum treatment). The perovskite film without MACl residue was prepared with thermal annealing at 60 °C for 2 h in a vacuum chamber. Measurements under AM1.5 solar continuous illumination (100 mW/cm^2) for 10 h.

Finally, we investigated the stability of devices incorporating the pore-free triiodide absorbers. All cells were tested unsealed in ambient air (45−50% humidity, 25 °C). Here, we find that MACl is responsible for rapid device degradation. Figure 4a,b presents X-ray photoelectron spectroscopy (XPS) data for perovskite films prepared from thermally annealing the film at 60 °C for 2 h in a glovebox and in vacuum chamber, respectively. Upon thermally annealing the film at 60 °C for 2 h in a glovebox (without vacuum treatment), the elemental contents of Pb, I, and Cl were (in atom percent) 10.4, 30.78, and 1.36%, respectively [Figure 4a], which we marked as "with MACl residue". When the perovskite film underwent thermal annealing inside a vacuum oven at 60 °C for 2 h, the content of Cl decreased below the detection limit of 0.01 atom % [Figure 4b], which was marked as "No MACl residue". Therefore, we conclude that within the detection depth of XPS (5−10 nm) in the films, chlorine content is removed by the vacuum assisted thermal annealing.

We observed very poor stability for the sample "with MACl residue". The perovskite film turned yellow when it was exposed to air for several hours (Supporting Information Figure S20), presumably due to a small amount of MACl absorbing water from the air, which subsequently decomposes the $CH_3NH_3PbI_3$ crystallites. The devices featuring MACl-containing perovskite absorbers also degraded quickly (<2 h, Figure 4c). In contrast, we observed almost no color change for our pore-free films of "No MACl residue" sample —even after they were exposed to air for more than one month (Supporting Information Figure S20). Furthermore, we also found that the presence of PCBM as an acid inert interface layer and Ag as an electrode can impede the halide corrosion (Supporting Information Figure S 21). Not surprisingly, our devices featuring an Ag electrode could sustain up to 10 days in air without corrosion of the film. As revealed in Figure 4c, d, the device performance after 10 h of continuous illumination remained stable, confirming that greatly improved stability could be achieved after the removal of MACl.

CONCLUSION

In conclusion, precise control over the composition and morphology of perovskite thin films produced from 3MAI:$PbCl_2$ is possible when using vacuum-assisted annealing, which promotes the removal of MACl, resulting in pure, pore-free, finely crystallized triiodide ($CH_3NH_3PbI_3$) films from a one-step solution deposition method. Highly efficient $CH_3NH_3PbI_3$ solar cells (PCE: 14.52%) can be obtained using this method, with very high reproducibility. Furthermore, through elimination of residual MACl from the $CH_3NH_3PbI_3$ film, we can enhance long-term stability of the perovskite solar cells and preventing notorious and unwanted hysteresis effects. Consequently, this new processing scheme allows the preparation of

excellent-quality triiodide ($CH_3NH_3PbI_3$) thin films. We anticipate that our findings will enable further improvements in the performance of the perovskite photovoltaic family.

METHODS

Materials. Anhydrous *N*,*N*-dimethylformamide (DMF, 99.8%), methylamine (CH_3NH_2, 33 wt % in EtOH), hydroiodic acid (HI, 57 wt % in H_2O), and $PbCl_2$ (99.999%) were purchased from Aldrich. $PC_{61}BM$ was obtained from Solarmer Material. Poly(9,9-bis[3′-(*N*,*N*-dimethyl)-*N*-ethylammoinium-propyl-2,7-fluorene]-*alt*-2,7-(9,9-dioctylfluorene)]dibromide-Electrolyte (PFN-Br) was purchased from 1-Material. CH_3NH_3I was synthesized according to the reported method.[15] Methylamine (33 wt % in EtOH; 20 mL) was diluted with absolute EtOH (100 mL) and then reacted with HI (57 wt % in water; 10 mL) in a 250 mL round-bottom flask, and cooled in an ice bath, for 2 h with stirring. A white precipitate was obtained after evaporation at 40 °C for 6 h in a vacuum chamber. The precursor solution was prepared by stirring CH_3NH_3I and $PbCl_2$ (molar ratio, 3:1) at room temperature for 24 h.

Device Fabrication. Devices were prepared on cleaned half-coated ITO substrates. First, a commercial aqueous dispersion of PEDOT:PSS (Clevios PVP AI 4083) was spin-coated (2000 rpm) on a precleaned ITO substrate, forming a PEDOT:PSS layer having a thickness of 40 nm. On top of this layer, perovskite layer was deposited from a DMF solution (50 wt %), forming a 300 nm-thick film. The film thickness was controlled by varying the concentration of the perovskite solution and the spin-coating speed. The substrates were then either thermally annealed in glovebox or transferred to a vacuum chamber and thermally annealed at a temperature from 60 to 100 °C under a pressure of 1 mbar. The samples in these processes should avoid exposure to air or other solvent vapors.

The PCBM layer was spin-coated (3000 rpm) from a chlorobenzene solution (20 mg/mL) in a N_2-filled glovebox. The PFN-Br layer was assembled on then PCBM layer from 0.2% MeOH solution. Ag electrode was thermally evaporated on top of the device under a base pressure of 3×10^{-4} mbar to a thickness of 150 nm, with a device area of 0.06 cm^2. The thickness of each layer was determined using a surface profiler.

Measurement and Characterization. Solar-simulated AM 1.5 sunlight was generated using a Newport AM 1.5G solar simulator (100 mW/cm^2), calibrated with an ISO 17025-certified KG3-filtered silicon reference cell. The spectral mismatch factor was calculated to be less than 1%. The *J*−*V* curves were recorded using a Keithley 2650 apparatus. Because the perovskite material had very high mobility, each unit of the cell was cut separately to ensure the accuracy of the measurement.

XPS was performed using a Physical Electronic 5600 multitechnique system (monochromatic Al Kα X-ray source). AFM was performed using a NanoScope III microscope (Digital Instrument) operated in tapping mode. SEM images were recorded using a Hitachi S-4800 microscope.

Time-resolved photoluminescence (PL) spectra of the samples were measured using a Hamamatsu Steak Scope C4334 apparatus. Femtosecond pump pulses were provided by the Coherent Model Mira 900 titanium:sapphire laser and frequency-doubled to 405 nm. The repetition rate of the output pulses from the laser was reduced to 4.75 MHz through use of a Coherent Model 9200 Pulse Picker. The pump fluence at the sample was approximately 1.33 μJ/cm^2/pulse. The PL lifetimes of the bare $CH_3NH_3PbI_3$ film on a PEDOT:PSS/ITO glass substrate was calculated by fitting the experimental decay transient data to the single-exponential decay model. The PL decay dynamics of the perovskite devices with a layer of PCBM on the active layer was also modeled according to the one-dimensional diffusion equation:

$$\frac{\partial n(x,t)}{\partial t} = D\frac{\partial^2 n(x,t)}{\partial x^2} - kn(x,t)$$

where $n(x,t)$ is the number and distribution of the laser pulse-generated charge carrier density in the active material film, D is the diffusion coefficient of the charge carrier, and k is the original charge carrier consumption rate in the absence of the PCBM layer.[11,12]

Conflict of Interest: The authors declare no competing financial interest.

Supporting Information Available: XPS elemental analysis, SEM images of the perovskite films, XRD spectrum of perovskite film, optical constants of perovskite film, *J*−*V* characteristics of perovskite solar cells, hysteresis measurement of perovskite solar cells, absorptions of perovskite films, IPCEs and integrated J_{sc} of perovskite solar cells. This material is available free of charge *via* the Internet at http://pubs.acs.org.

Acknowledgment. This study was supported by the University Grant Council of the University of Hong Kong (Grants 10401466 and 201111159062), the General Research Fund (Grants HKU711813 and HKU711612E), an RGC-NSFC Grant (N_HKU709/12), the Collaborative Research Fund (grant CUHK1/CRF/12G) from the Research Grants Council of Hong Kong Special Administrative Region, China, and Grant CAS14601 from CAS-Croucher Funding Scheme for Joint Laboratories. MG thanks the European Research Council (ERC) for an Advanced Research Grant (ARG 247404) funded under his "'Mesolight'" project and the Swiss National Science foundation for financial support under the Nanotera Synergy project no 530138. K.S. would like to acknowledge the financial support of AoE/P-02/12 the Research Grants Council.

REFERENCES AND NOTES

1. Park, S. H.; Roy, A.; Beaupre, S.; Cho, S.; Coates, N.; Moon, J. S.; Moses, D.; Leclerc, M.; Lee, K.; Heeger, A. J. Bulk Heterojunction Solar Cells with Internal Quantum Efficiency Approaching 100%. *Nat. Photonics* **2009**, *3*, 297–302.
2. Liang, Y.; Xu, Z.; Xia, J.; Tsai, S.-T.; Wu, Y.; Li, G.; Ray, C.; Yu, L. For the Bright Future—Bulk Heterojunction Polymer Solar Cells with Power Conversion Efficiency of 7.4%. *Adv. Mater.* **2010**, *22*, E135–E138.
3. Xie, F.; Choy, W. C. H.; Wang, C.; Li, X.; Zhang, S.; Hou, J. Low-Temperature Solution-Processed Hydrogen Molybdenum and Vanadium Bronzes for an Efficient Hole-Transport Layer in Organic Electronics. *Adv. Mater.* **2013**, *25*, 2051–2055.
4. Chen, C.-C.; Chang, W.-H.; Yoshimura, K.; Ohya, K.; You, J.; Gao, J.; Hong, Z.; Yang, Y. An Efficient Triple-Junction Polymer Solar Cell Having a Power Conversion Efficiency Exceeding 11%. *Adv. Mater.* **2014**, *25*, 5670–5677.
5. Li, X.; Choy, W. C.; Xie, F.; Zhang, S.; Hou, J. Room-temperature Solution-Processed Molybdenum Oxide as a Hole Transport Layer with Ag Nanoparticles for Highly Efficient Inverted Organic Solar Cells. *J. Mater. Chem. A* **2013**, *1*, 6614–6621.
6. Burschka, J.; Pellet, N.; Moon, S.-J.; Humphry-Baker, R.; Gao, P.; Nazeeruddin, M. K.; Gratzel, M. Sequential Deposition as a Route to High-Performance Perovskite-Sensitized Solar Cells. *Nature* **2013**, *499*, 316–319.
7. Liu, M.; Johnston, M. B.; Snaith, H. J. Efficient Planar Heterojunction Perovskite Solar Cells by Vapour Deposition. *Nature* **2013**, *501*, 395–398.
8. Liu, D.; Kelly, T. L. Perovskite Solar Cells with a Planar Heterojunction Structure Prepared Using Room-Temperature Solution Processing Techniques. *Nat. Photonics* **2014**, *8*, 133–138.
9. Park, N.-G. Organometal Perovskite Light Absorbers Toward a 20% Efficiency Low-Cost Solid-State Mesoscopic Solar Cell. *J. Phys. Chem. Lett.* **2013**, *4*, 2423–2429.
10. Wang, Q.; Shao, Y.; Dong, Q.; Xiao, Z.; Yuan, Y.; Huang, J. Large Fill-Factor Bilayer Iodine Perovskite Solar Cells

Fabricated by a Low-Temperature Solution-Process. *Energy Environ. Sci.* **2014**, *7*, 2359–2365.
11. Xing, G.; Mathews, N.; Sun, S.; Lim, S. S.; Lam, Y. M.; Grätzel, M.; Mhaisalkar, S.; Sum, T. C. Long-Range Balanced Electron- and Hole-Transport Lengths in Organic-Inorganic $CH_3NH_3PbI_3$. *Science* **2013**, *342*, 344–347.
12. Stranks, S. D.; Eperon, G. E.; Grancini, G.; Menelaou, C.; Alcocer, M. J. P.; Leijtens, T.; Herz, L. M.; Petrozza, A.; Snaith, H. J. Electron-Hole Diffusion Lengths Exceeding 1 Micrometer in an Organometal Trihalide Perovskite Absorber. *Science* **2013**, *342*, 341–344.
13. Ponseca, C. S.; Savenije, T. J.; Abdellah, M.; Zheng, K.; Yartsev, A.; Pascher, T.; Harlang, T.; Chabera, P.; Pullerits, T.; Stepanov, A.; *et al.* Organometal Halide Perovskite Solar Cell Materials Rationalized: Ultrafast Charge Generation, High and Microsecond-Long Balanced Mobilities, and Slow Recombination. *J. Am. Chem. Soc.* **2014**, *136*, 5189–5192.
14. Wehrenfennig, C.; Eperon, G. E.; Johnston, M. B.; Snaith, H. J.; Herz, L. M. High Charge Carrier Mobilities and Lifetimes in Organolead Trihalide Perovskites. *Adv. Mater.* **2014**, *26*, 1584–1589.
15. Lee, M. M.; Teuscher, J.; Miyasaka, T.; Murakami, T. N.; Snaith, H. J. Efficient Hybrid Solar Cells Based on Meso-Superstructured Organometal Halide Perovskites. *Science* **2012**, *338*, 643–647.
16. Son, D.-Y.; Im, J.-H.; Kim, H.-S.; Park, N.-G. 11% Efficient Perovskite Solar Cell Based on ZnO Nanorods: An Effective Charge Collection System. *J. Phys. Chem. C* **2014**, *118*, 16567–16573.
17. Nanova, D.; Kast, A. K.; Pfannmöller, M.; Müller, C.; Veith, L.; Wacker, I.; Agari, M.; Hermes, W.; Erk, P.; Kowalsky, W.; *et al.* Unraveling the Nanoscale Morphologies of Mesoporous Perovskite Solar Cells and Their Correlation to Device Performance. *Nano Lett.* **2014**, *14*, 2735–2740.
18. Kim, H.-S.; Lee, C.-R.; Im, J.-H.; Lee, K.-B.; Moehl, T.; Marchioro, A.; Moon, S.-J.; Humphry-Baker, R.; Yum, J.-H.; Moser, J. E.; *et al.* Lead Iodide Perovskite Sensitized All-Solid-State Submicron Thin Film Mesoscopic Solar Cell with Efficiency Exceeding 9%. *Sci. Rep.* **2012**, *2*, 591.
19. Jeng, J.-Y.; Chiang, Y.-F.; Lee, M.-H.; Peng, S.-R.; Guo, T.-F.; Chen, P.; Wen, T.-C. $CH_3NH_3PbI_3$ Perovskite/Fullerene Planar-Heterojunction Hybrid Solar Cells. *Adv. Mater.* **2013**, *25*, 3727–3732.
20. Kim, H.-B.; Choi, H.; Jeong, J.; Kim, S.; Walker, B.; Song, S.; Kim, J. Y. Mixed Solvents for the Optimization of Morphology in Solution-Processed, Inverted-Type Perovskite/Fullerene Hybrid Solar Cells. *Nanoscale* **2014**, *6*, 6679–6683.
21. Conings, B.; Baeten, L.; De Dobbelaere, C.; D'Haen, J.; Manca, J.; Boyen, H.-G. Perovskite-Based Hybrid Solar Cells Exceeding 10% Efficiency with High Reproducibility Using a Thin Film Sandwich Approach. *Adv. Mater.* **2014**, *26*, 2041–2046.
22. You, J.; Hong, Z.; Yang, Y.; Chen, Q.; Cai, M.; Song, T.-B.; Chen, C.-C.; Lu, S.; Liu, Y.; Zhou, H.; *et al.* Low-Temperature Solution-Processed Perovskite Solar Cells with High Efficiency and Flexibility. *ACS Nano* **2014**, *8*, 1674–1680.
23. Liang, P.-W.; Liao, C.-Y.; Chueh, C.-C.; Zuo, F.; Williams, S. T.; Xin, X.-K.; Lin, J.; Jen, A. K. Y. Additive Enhanced Crystallization of Solution-Processed Perovskite for Highly Efficient Planar-Heterojunction Solar Cells. *Adv. Mater.* **2014**, *26*, 3748–3754.
24. Sun, S.; Salim, T.; Mathews, N.; Duchamp, M.; Boothroyd, C.; Xing, G.; Sum, T. C.; Lam, Y. M. The Origin of High Efficiency in Low-Temperature Solution-Processable Bilayer Organometal Halide Hybrid Solar Cells. *Energy Environ. Sci.* **2014**, *7*, 399–407.
25. Dualeh, A.; Tétreault, N.; Moehl, T.; Gao, P.; Nazeeruddin, M. K.; Grätzel, M. Effect of Annealing Temperature on Film Morphology of Organic–Inorganic Hybrid Pervoskite Solid-State Solar Cells. *Adv. Funct. Mater.* **2014**, *24*, 3250–3258.
26. Yu, H.; Wang, F.; Xie, F.; Li, W.; Chen, J.; Zhao, N. The Role of Chlorine in the Formation Process of "$CH_3NH_3PbI_{3-x}Cl_x$" Perovskite. *Adv. Funct. Mater.* **2014**, *24*, 7102–7108.
27. Tidhar, Y.; Edri, E.; Weissman, H.; Zohar, D.; Hodes, G.; Cahen, D.; Rybtchinski, B.; Kirmayer, S. Crystallization of Methyl Ammonium Lead Halide Perovskites: Implications for Photovoltaic Applications. *J. Am. Chem. Soc.* **2014**, *136*, 13249–13256.
28. Niu, G.; Li, W.; Meng, F.; Wang, L.; Dong, H.; Qiu, Y. Study on the Stability of $CH_3NH_3PbI_3$ Films and the Effect of Post-Modification by Aluminum Oxide in All-Solid-State Hybrid Solar Cells. *J. Mater. Chem. A* **2014**, *2*, 705–710.
29. Zhou, H.; Chen, Q.; Li, G.; Luo, S.; Song, T.-b.; Duan, H.-S.; Hong, Z.; You, J.; Liu, Y.; Yang, Y. Interface Engineering of Highly Efficient Perovskite Solar Cells. *Science* **2014**, *345*, 542–546.
30. Zhao, Y.; Zhu, K. Efficient Planar Perovskite Solar Cells Based on 1.8 eV Band Gap CH3NH3PbI2Br Nanosheets *via* Thermal Decomposition. *J. Am. Chem. Soc.* **2014**, *136*, 12241–12244.
31. Malinkiewicz, O.; Yella, A.; Lee, Y. H.; Espallargas, G. M.; Graetzel, M.; Nazeeruddin, M. K.; Bolink, H. J. Perovskite Solar Cells Employing Organic Charge-Transport Layers. *Nat. Photonics* **2014**, *8*, 128–132.
32. Xing, G.; Mathews, N.; Lim, S. S.; Yantara, N.; Liu, X.; Sabba, D.; Grätzel, M.; Mhaisalkar, S.; Sum, T. C. Low-Temperature Solution-Processed Wavelength-Tunable Perovskites for Lasing. *Nat. Mater.* **2014**, *13*, 476–480.
33. Xiao, Z.; Bi, C.; Shao, Y.; Dong, Q.; Wang, Q.; Yuan, Y.; Wang, C.; Gao, Y.; Huang, J. Efficient, High Yield Perovskite Photovoltaic Devices Grown by Interdiffusion of Solution-Processed Precursor Stacking Layers. *Energy Environ. Sci.* **2014**, *7*, 2619–2623.
34. Snaith, H. J.; Abate, A.; Ball, J. M.; Eperon, G. E.; Leijtens, T.; Noel, N. K.; Stranks, S. D.; Wang, J. T.-W.; Wojciechowski, K.; Zhang, W. Anomalous Hysteresis in Perovskite Solar Cells. *J. Phys. Chem. Lett.* **2014**, *5*, 1511–1515.